Journal of Sound and Vibration (2001) **240**(3), 519–543
doi:10.1006/jsvi.2000.3247, available online at http://www.idealibrary.com on IDEAL®

VIBRATION ANALYSIS OF HYPOID TRANSMISSIONS APPLYING AN EXACT GEOMETRY-BASED GEAR MESH THEORY

Y. CHENG†

Department of Mechanical Engineering, The Ohio State University, 206 West 18th Avenue, Columbus, OH 43210, U.S.A.

AND

T. C. LIM

Department of Mechanical Engineering 290 Hardaway Hall, Box 870276, The University of Alabama, Tuscaloosa, AL 35487, U.S.A., E-mail: tlim@coe.eng.ua.edu

(*Received* 8 *November* 1999, *and in final form* 13 *July* 2000)

A new kinematic model based on exact gear geometry that is derivable from a set of manufacturing parameters is developed for analyzing the hypoid gear-mesh-coupling mechanism. The approach involves a discretization of the contact lines in the plane of action assuming an unperturbed quasi-static gear meshing state to obtain the effective mesh excitation and position vectors. This mesh formulation forms the basis for a three-dimensional multiple-degrees-of-freedom (d.o.f.s) dynamic model of the hypoid gear pair, which is used to simulate the rotation and translation response spectra due to the harmonically driven transmission error excitation. From the free and forced vibration results, the unique elastic modes that contribute to the generation of gear-mesh-induced vibrations are identified. The mesh force response function is also analyzed to examine the sensitivity of dynamic coupling and vibratory response to critical design parameters. This study demonstrates the superiority of the proposed theory compared to the simpler gear-mesh representations utilized in previous studies, and leads to the conclusion that all 6 d.o.f.s of each gear body must be modelled explicitly. Numerous parametric studies are performed to quantify the dependence of vibration modes and response trends to selected design values and operating conditions.

1. INTRODUCTION

The hypoid rear set is widely used in the rear axles of passenger cars and trucks to transmit rotational motion in perpendicular directions. The gears in this application are often subjected to a harmful dynamic response that can cause gear whine annoyance and structural fatigue problems. It is generally known that the gear kinematic transmission error is the primary source of the vibratory energy excitation. There have been extensive studies performed on the synthesis of machine tool and cutter settings to manufacture higher precision pinion and gear profiles, and optimization of mesh patterns by applying tooth contact analysis to minimize transmission errors [1–8]. However, very limited effort has been directed at the modelling and dynamic analysis of the hypoid or related bevel (that

†Currently with Optimal CAE Inc., Novi. MI, U.S.A.

0022-460X/01/080519 + 25 $35.00/0

is essentially a hypoid design with no offset) gear pair, even though the dynamics of parallel axis gears have been investigated extensively [9–12]. Thus so far, an integrated and exact dynamic model for the hypoid-geared rotor system does not exist. Hence, several experimentally observed phenomena remain unexplained, such as the measured difference in the dynamic characteristics under drive and coast conditions, and the nature of torsional and translational vibration coupling.

The limited studies reported in the open literature on hypoid gear dynamics are mostly based on either experimental observation or simple semi-empirical formulation. For instance, one of the earlier attempts by Remmers [13] used a lumped parameter model to simulate the torsional response of the rear axle driveline containing a hypoid set, and identified the pinion resonance spectrum assuming infinite mesh stiffness. Later, Kiyono *et al.* [14] derived an analytical two-degrees-of-freedom (d.o.f.s) model of a bevel gear pair using an assumed pattern of the line-of-action vector, and studied the system stability characteristics. At about the same time, Terauchi *et al.* [15] published some experimental data in the form of dynamic load, torque fluctuation and shaft bending vibration responses containing system resonant frequency information for the simpler straight bevel gears. Later, Fang [16] developed a lumped parameter vibration model of a spiral bevel gear transmission to compute dynamic load and gear response. His mesh model is based on the classical gear mesh force equations that produce a simple unidirectional gear-mesh-coupling vector. Furthermore, Nakayashiki *et al.* [17] showed a direct correlation between the torsional vibration response of a hypoid set in a rear axle driveline assembly, which is affected by the pinion shaft compliance and bearing stiffness, and gear whine level. Recently, Abe and Hagiwara [18] demonstrated experimentally that hypoid gear noise from a specific design could be reduced by tuning driveline vibration modes through the addition of an inertia mass on the side-flanges of the output shaft. In another experimental study, Hirasaka *et al.* [19] developed a method to estimate the dynamic mesh force of a hypoid gear pair using the measured data, and predicted that lowering propeller shaft stiffness could reduce gear mesh force significantly in some cases. The most practical model prior to the present study was suggested by Donley *et al.* [20] who proposed an approximate hypoid gear mesh formulation for the use in the context of a dynamic finite element representation. Their approximate formulation relies on the assumption of a mean pitch point location and is based on a bevel gear mesh equivalence theory. None of the above studies clearly defines the hypoid gear mesh coupling precisely, and the models essentially rely on simplified mesh force vector. Furthermore, only torsional vibrations were usually modelled. It is quite clear that a more precise hypoid gear mesh formulation, which is directly related to the gear design parameters and capable of modelling the translation and rotation vibrations simultaneously, is needed.

This paper presents a new analytical derivation of the hypoid gear-mesh-coupling mechanism based on the simulation of tooth contact assuming idealized gear geometry. The proposed theory is incorporated into a three-dimensional (3D) elastically coupled rigid-body dynamic model, which is applied to compute the dynamic characteristics of a generic hypoid geared rotor system subjected to transmission error excitation. The dynamic model is also used to analyze the mesh-force-coupling phenomenon and the transmissibility of the gear mesh excitation and externally applied loads through the gear mesh interface.

2. KINEMATICS

Given the complete machine and cutter settings, the geometry of the pinion and gear surfaces can be generated theoretically using the numerical space gearing method

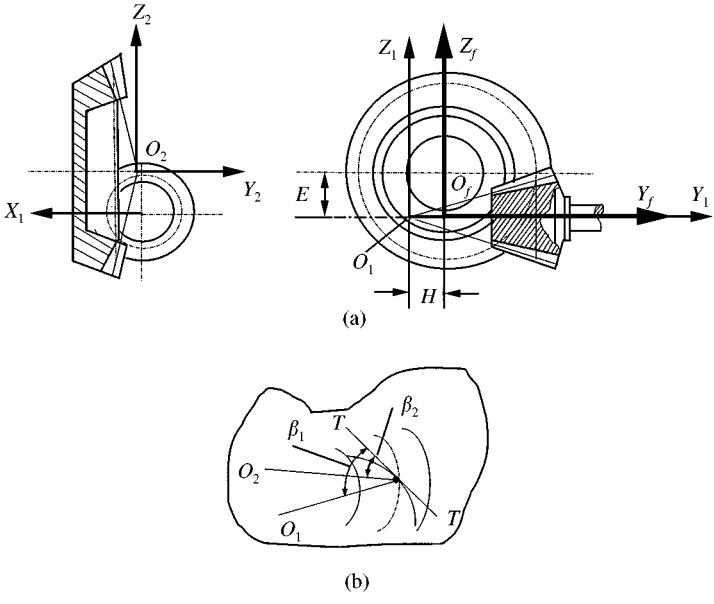

Figure 1. (a) Hypoid gear co-ordinate systems S_f and S_l ($l = 1, 2$) used in tooth contact simulation; distance E defines the pinion offset, H is the pitch apex O_1 beyond cross point O_f, and axes Y_1 and Y_2 represent rotation centerlines for the pinion and gear respectively. (b) Pitch plane and spiral angles.

[1,6,21–27]. This approach is applied here because an explicit mathematical representation of the hypoid tooth profile generally does not exist unlike the tooth forms of spur and helical gears. It may be noted that a hypoid gear pair with true conjugate action theoretically produces line contact form. In order to decrease the sensitivity of the mesh to manufacturing or assembly error, a certain amount of tooth modification is usually applied to the gear teeth. Hence, point contact occurs between the mating teeth rather than line one, which actually become more elliptical under load. In the following derivation, the theoretical contact is assumed to concentrate at a single point that represents the mean contact position.

Consider three Cartesian co-ordinate systems fixed to the frame, pinion and gear components, respectively, as shown in Figure 1. The co-ordinate system fixed to the frame is assumed inertial and denoted by $S_f(x_f, y_f, z_f)$. The other two co-ordinates are given by $S_l(x_l, y_l, z_l)$, where subscript $l = 1, 2$, are rigidly connected to the driving pinion and driven gear, respectively, in which both Y_l axes define the operating rotational directions. Based on a method similar to those used by references [1,23–27], the tooth surface Σ_l may be represented in S_l by the vector function

$$\mathbf{r}^{(l)}(s_l, v_l) \subset C^2, \quad \mathbf{r}_{s_l}^{(l)} \times \mathbf{r}_{v_l}^{(l)} \neq 0, \tag{1}$$

where s_l and v_l are the surface co-ordinates, C^2 refers to the class of function $\mathbf{r}^{(l)}$ that possesses continuous derivatives up to the second order, and

$$\mathbf{r}_{s_l}^{(l)} = \frac{\partial \mathbf{r}^{(l)}}{\partial s_l}, \quad \mathbf{r}_{v_l}^{(l)} = \frac{\partial \mathbf{r}^{(l)}}{\partial v_l}. \tag{2}$$

Here the superscript (l) in parenthesis refers to the specific gear number, while the subscript l indicates the reference co-ordinate system. Accordingly, the surface normal vector $\mathbf{N}^{(l)}$ and

the corresponding unit normal vector $\mathbf{n}^{(l)}$ are given by

$$\mathbf{N}^{(l)} = \mathbf{r}_{s_l}^{(l)} \times \mathbf{r}_{v_l}^{(l)}, \quad \mathbf{n}^{(l)} = \frac{\mathbf{N}^{(l)}}{|\mathbf{N}^{(l)}|}. \tag{3}$$

The tooth surface Σ_1 of the pinion that rotates about Y_1 can be represented as a family of curved surfaces in S_f given by

$$\mathbf{r}_f^{(1)} = [M_{f1}]\mathbf{r}_1^{(l)} = \mathbf{r}_f^{(l)}(s_1, v_1, \varphi_1'), \tag{4}$$

where $[M_{fl}]$ is the transformation matrix from S_l to S_f, and φ_1' is the instantaneous roll angle of the pinion. The unit normal vector of Σ_1 can also be expressed as

$$\mathbf{n}_f^{(1)} = [M_{f1}]\mathbf{n}_1^{(1)} = \mathbf{n}_f^{(1)}(s_1, v_1, \varphi_1'). \tag{5}$$

Similarly, the mating gear that rotates about Y_2 with the tooth surface Σ_2 can be defined in S_f by

$$\mathbf{r}_f^{(2)} = [M_{f2}]\mathbf{r}_2^{(2)} = \mathbf{r}_f^{(2)}(s_2, v_2, \varphi_2'), \tag{6}$$

$$\mathbf{n}_f^{(2)} = [M_{f2}]\mathbf{n}_2^{(2)} = \mathbf{n}_f^{(2)}(s_2, v_2, \varphi_2'). \tag{7}$$

During the gear meshing process, the tooth surfaces Σ_1 and Σ_2 must be in continuous tangency as shown by line T–T in Figure 1, and therefore they must have a common contact point and normal vector. By enforcing this condition, the following two equations can then be obtained:

$$\mathbf{r}_f^{(1)}(s_1, v_1, \varphi_1') = \mathbf{r}_f^{(2)}(s_2, v_2, \varphi_2'), \quad \mathbf{n}_f^{(1)}(s_1, v_1, \varphi_1') = \mathbf{n}_f^{(2)}(s_2, v_2, \varphi_2'), \tag{8, 9}$$

where φ_2' is the instantaneous roll angle of the gear member. It should be noted that $|\mathbf{n}_f^{(1)}| = |\mathbf{n}_f^{(2)}| = 1$. Thus, the above pair of equations provides a system of five independent scalar equations

$$f_j(s_1, v_1, \varphi_1', s_2, v_2, \varphi_2') = 0, \quad j = 1, 2, 3, 4, 5. \tag{10}$$

These five non-linear algebraic equations can be solved numerically using a standard iterative method. In our study, a modified Powell–Hybrid algorithm is used in which a forward-difference approximation to the Jacobian matrix is applied. The solution will determine the relationships between the roll angles of the gear members, path of contact, transmission error as well as meshing position and normal vectors for any angular position.

The detailed generation of the pinion and gear tooth surfaces is described in references [1,25,27]. The corresponding matrices in the above equations are provided explicitly in Appendix A. Subsequently, the instantaneous kinematic transmission error can be computed from

$$e(\varphi_1') = (\varphi_2' - \varphi_2^*) - \frac{N_1}{N_2}(\varphi_1' - \varphi_1^*), \tag{11}$$

where φ_1^* and φ_2^* are initial roll angles of the pinion and gear at the theoretical mean position, and N_1 and N_2 are pinion and gear tooth numbers respectively. This formulation

TABLE 1

Hypoid gear design parameters

Blank data	
Number of teeth	10 (pinion)
	43 (gear)
Face width (mm)	48
Pinion offset (mm, below)	31·75
Mean cone distance (mm)	152·14
Gear face angle	1·2834
Gear root angle	1·2322
Gear addendum (mm)	3·41
Gear dedendum (mm)	10·42
Gear machine and cutter setting	
Machine root angle	1·2287
Machine center to back (mm)	1·270
Horizontal setting (mm)	85·598
Vertical setting (mm)	96·177
Cutter blade angle	0·3927
Nominal radius (mm)	114·30
Point width (mm)	3·81
Pinion machine and cutter settings	
Cutter blade angle	0·3491
Machine root angle	− 0·0226
Machine center to back (mm)	− 4·5847
Point radius (mm)	108·450
Basic swivel angle	− 0·7046
Radial setting (mm)	118·513
Basic cradle angle	1·0614
Blank offset (mm)	24·542
Sliding base (mm)	18·242
Ratio of roll	3·9936

is a significant improvement over the simpler mesh model [13,18,20] used in earlier dynamic simulations. The earlier models essentially assume the mesh line of action to be $\mathbf{n}_f = \{0, 0, \pm 1\}^{\mathrm{T}}$, where the negative sign refers to the forward drive while the positive sign is for the coast case, which does not produce any observable difference in the system dynamic response.

The above computational procedure is then applied to a pair of hypoid gear set that is suitable for automotive application. In this case, the forward driving mesh encompasses the concave side of the pinion and the convex side of the gear. Its corresponding manufacturing parameters are given in Table 1. The predicted kinematic transmission error in degrees based on equation (11) is shown in Figure 2 for three mesh cycles in terms of pinion roll angle. From this numerical exercise, it is clear that the tooth mesh simulation depends on the machine tool settings and cutter information as well as the exact mathematical representation of the generation process, unlike the earlier model. Also note that the formulation can readily compute the effects of temporal and spatial-varying mesh parameters in the case where the mesh representation is not reduced to a discrete representation. On the other hand, if a time-invariant mesh formulation is of interest, a more primitive method based on the pitch cone design concept can be applied as suggested by references [25–28]. For the case in Table 1, the effective mesh position and normal vectors obtained from these two approaches are compared in Table 2. The results of

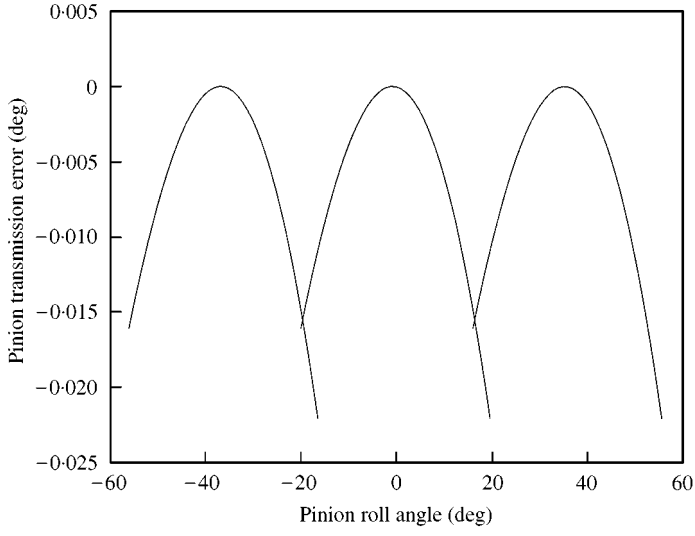

Figure 2. Kinematic transmission error of the hypoid gear pair obtained from the mesh simulation.

TABLE 2

Comparison of the position and normal vectors of the effective mesh point obtained from pitch cone equation and the proposed quasi-static tooth mesh simulation between concave side of the pinion and convex side of the gear

Method	x_f (mm)	y_f (mm)	z_f (mm)	n_{xf}	n_{yf}	n_{zf}
Pitch-cone equation	− 40·31	142·31	2·532	− 0·1896	− 0·7468	− 0·6474
Proposed theory	− 40·32	140·51	2·702	− 0·1797	− 0·7448	− 0·6426
Difference (%)	0·02	1·3	6·7	5·2	0·3	0·7

both calculations are nearly equal at the pitch point, which indirectly provided a partial validation of our proposed theory. Since our derivation includes a more precise mesh characteristics, it is assumed to be more superior and in fact provides a basis for modelling non-linear time-varying behavior that is normally more prominent in lightly loaded condition. The calculated mesh position and line of action vectors will be used in the development of the dynamic model in the subsequent section. The dynamic response calculations performed in this paper will be limited to linear cases only since the present intent is to examine the nature of the mesh coupling from the system perspective for high steady state torque input.

3. DYNAMIC MODELLING

3.1. GEAR MESH FORMULATION

Consider a generic driveline system comprising a hypoid gear pair, an engine inertia and a load element as shown in Figure 3, which is an idealization of a typical hypoid-geared-rotor system. Each gear is modelled as a rigid conical body attached to a torsionally flexible shaft, which is supported by a compliant rolling element bearing

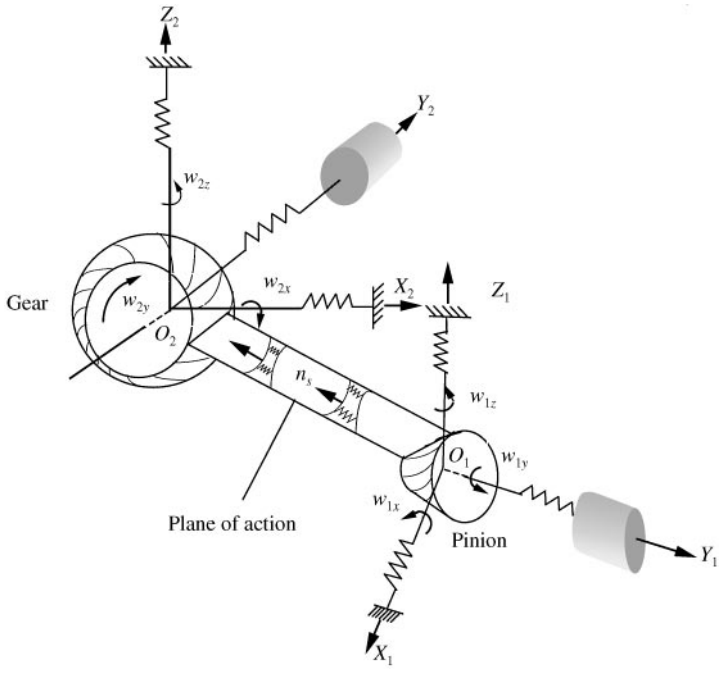

Figure 3. A dynamic model of a hypoid gear transmission. (Note that torsional springs are not shown to avoid clutter in the sketch.)

represented by a set of discrete stiffness and damping elements [29] in the centroids of the gear bodies. The nominal rotations of the pinion and gear are about Y_1 and Y_2, respectively, as mentioned earlier. Furthermore, only the torsional co-ordinates of the engine and the load are modelled as they are normally decoupled from the gear set in the translational directions by design. The elastic gear mesh coupling is represented by an oblique, proportionally damped mesh spring. It is also the source of displacement-type excitation caused by transmission error, which generates internal dynamic mesh forces and moments acting on the centroids of the gear bodies. These concepts are basically extrapolated from previous parallel axis gear models as described in references [9,11,12,30].

To define a mathematical representation of the mesh-coupling stiffness, the contact area in the plane of action is discretized into a series of cells containing the localized stiffness k_s that is a function of the spatial dimensions. The positional vectors of each contact cell in the local coordinate system $S_l (l = 1, 2)$ is $\mathbf{R}_s^{(l)} = [x_s^{(l)} y_s^{(l)} z_s^{(l)}]^{\mathrm{T}}$ and the unit normal vector is given by $\mathbf{n}_s^{(l)} = [n_{sx}^{(l)}, n_{sy}^{(l)}, n_{sz}^{(l)}]^{\mathrm{T}}$. The projection of the normal vector into the tangential direction of rotational motion relative to the X_l–Y_l–Z_l co-ordinate system can be expressed in the vector and reduced scalar forms as

$$\lambda_{sx}^{(l)} = \mathbf{n}_s^{(l)} \cdot (\mathbf{i}^{(l)} \times \mathbf{R}_s^{(l)}), \quad \lambda_{sy}^{(l)} = \mathbf{n}_s^{(l)} \cdot (\mathbf{j}^{(l)} \times \mathbf{R}_s^{(l)}), \quad \lambda_{sz}^{(l)} = \mathbf{n}_s^{(l)} \cdot (\mathbf{k}^{(l)} \times \mathbf{R}_s^{(l)}), \tag{12a}$$

$$\lambda_{sx}^{(l)} = n_{sz}^{(l)} y_s^{(l)} - n_{sy}^{(l)} z_s^{(l)}, \quad \lambda_{sy}^{(l)} = n_{sx}^{(l)} z_s^{(l)} - n_{sz}^{(l)} x_s^{(l)}, \quad \lambda_{sz}^{(l)} = n_{sy}^{(l)} x_s^{(l)} - n_{sx}^{(l)} y_s^{(l)}, \tag{12b}$$

respectively, where $\mathbf{i}^{(l)}$, $\mathbf{j}^{(l)}$ and $\mathbf{k}^{(l)}$ are the triad of unit vectors that defines the co-ordinate system S_l. The directional cosine of cell s depends on the gear geometry and position of the

cell, and can be written in the vector and reduced scalar forms relative to S_l as

$$\mathbf{h}_s^{(l)}(t) = \left\{ \mathbf{n}_s^{(l)} \cdot \mathbf{i}^{(l)}, \mathbf{n}_s^{(l)} \cdot \mathbf{j}^{(l)}, \mathbf{n}_s^{(l)} \cdot \mathbf{k}^{(l)}, \frac{\mathbf{n}_s^{(l)} \cdot (\mathbf{i}^{(l)} \times \mathbf{R}_s^{(l)})}{R_{sx}^{(l)}}, \frac{\mathbf{n}_s^{(l)} \cdot (\mathbf{j}^{(l)} \times \mathbf{R}_s^{(l)})}{R_{sy}^{(l)}}, \frac{\mathbf{n}_s^{(l)} \cdot (\mathbf{k}^{(l)} \times \mathbf{R}_s^{(l)})}{R_{sz}^{(l)}} \right\}, \quad (13a)$$

$$\mathbf{h}_s^{(l)} = \{ n_{sx}^{(l)}\ n_{sy}^{(l)}\ n_{sz}^{(l)}\ \xi_{sx}^{(l)}\ \xi_{sy}^{(l)}\ \xi_{sz}^{(l)} \}, \quad (13b)$$

where $\xi_{sj}^{(l)} = \lambda_{sj}^{(l)} / R_{sj}^{(l)}$ for $j = x, y, z$, and $R_j^{(l)}$ denotes rotational radius computed from $R_{sx}^{(l)} = \|\mathbf{i}^{(l)} \times \mathbf{R}_s^{(l)}\|$, $R_{sy}^{(l)} = \|\mathbf{j}^{(l)} \times \mathbf{R}_s^{(l)}\|$ and $R_{sz}^{(l)} = \|\mathbf{k}^{(l)} \times \mathbf{R}_s^{(l)}\|$. Therefore, the normal approach defined as the translational deformation in the plane of action, which is usually referred to as the dynamic transmission error, can be written in vector form as

$$\delta_s(t) = \mathbf{h}_s^{(2)}(t) \cdot \mathbf{q}_2(t) - \mathbf{h}_s^{(l)}(t) \cdot \mathbf{q}_1(t), \quad (14)$$

where $\mathbf{q}_l(t) = \{x_l\ y_l\ z_l\ w_{xl}\ w_{yl}\ w_{zl}\}^{\mathrm{T}}$ is the vibratory displacement vector for each gear relative to S_l. Here x_l, y_l and z_l are the translational displacements and w_{xl}, w_{yl} and w_{zl} are the angular ones where $l = 1, 2$ corresponding to the specific gear member under consideration.

3.2. EQUATIONS OF MOTIONS

It is assumed that the gears contact continually and thus there is no loss of tooth contact. If we set the number of contact cells to be N_c whose localized spatially dependent stiffness is k_s, then it can be shown that the equation of vibratory motions for the pinion and gear can be expressed in matrix form as

$$[M_1]\{\ddot{q}_1\} - \sum_{s=1}^{N_c} c_s[\dot{\Delta}_s^{(1)}] - \sum_{s=1}^{N_c} k_s[\Delta_s^{(1)}] + [C_{1b}]\{\dot{q}_1\} + [K_{1b}]\{q_1\} = \{F_1\}, \quad (15a)$$

$$[M_2]\{\ddot{q}_2\} + \sum_{s=1}^{N_c} c_s[\dot{\Delta}_s^{(2)}] + \sum_{s=1}^{N_c} k_s[\Delta_s^{(2)}] + [C_{2b}]\{\dot{q}_2\} + [K_{2b}]\{q_2\} = \{F_2\}, \quad (15b)$$

$$[\Delta_s^{(i)}] = \mathbf{h}_s^{(i)^{\mathrm{T}}} \mathbf{h}_s^{(2)}\{q_2\} - \mathbf{h}_s^{(i)^{\mathrm{T}}} \mathbf{h}_s^{(1)}\{q_1\}. \quad (15c)$$

From the above equations, the stiffness matrices can be expressed explicitly as

$$[K_{11}] = \sum_{s=1}^{N_c} k_s \mathbf{h}_s^{(1)^{\mathrm{T}}} \mathbf{h}_s^{(1)}, \quad [K_{12}] = -\sum_{s=1}^{N_c} k_s \mathbf{h}_s^{(1)^{\mathrm{T}}} \mathbf{h}_s^{(2)}, \quad (16a, b)$$

$$[K_{21}] = -\sum_{s=1}^{N_c} k_s \mathbf{h}_s^{(2)^{\mathrm{T}}} \mathbf{h}_s^{(1)}, \quad [K_{22}] = \sum_{s=1}^{N_c} k_s \mathbf{h}_s^{(2)^{\mathrm{T}}} \mathbf{h}_s^{(2)}, \quad (16c, d)$$

Next, equation (15) can be assumed with the dynamical equations of the motor w_E and output load w_o co-ordinates to obtain a system model of dimension 14, which is given in the classical second order differential equation form as

$$[M]\ddot{q} + [C]\dot{q} + [K]q = \{F(t)\}, \quad (17)$$

where $\mathbf{q} = \{w_E\ q_1^{\mathrm{T}}\ w_o\ q_2^{\mathrm{T}}\}^{\mathrm{T}}$ is the system vibratory displacement vector. The system matrices are given by

$$[M] = \begin{bmatrix} M_1 & 0 \\ 0 & M_2 \end{bmatrix}, \quad [C] = [C_e] + [C_b], \quad [K] = [K_e] + [K_b]. \quad (18a–c)$$

Furthermore, the sub-matrices M_l associated with each gear is diagonal based on the lumped parameter formulation, and are explicitly given by

$$[M_1] = diag\left[\frac{I_E}{R_{py}^2} \quad m_p \quad m_p \quad m_p \quad \frac{I_{px}}{R_{px}^2} \quad \frac{I_{py}}{R_{py}^2} \quad \frac{I_{pz}}{R_{pz}^2}\right], \tag{19a}$$

$$[M_2] = diag\left[\frac{I_O}{R_{gy}^2} \quad m_g \quad m_g \quad m_g \quad \frac{I_{gx}}{R_{gx}^2} \quad \frac{I_{gy}}{R_{gy}^2} \quad \frac{I_{gz}}{R_{gz}^2}\right], \tag{19b}$$

where m_l is the mass term, I_{li} $(i = x, y, z)$ refers to the mass moment of inertia term, and R_{li} denotes the equivalent rotational radius. Thus, the mesh coupling and support stiffness matrices in equation (18) can be simply expressed as

$$[K_e] = \begin{bmatrix} K_{11}^* & K_{12}^* \\ K_{21}^* & K_{22}^* \end{bmatrix}, \quad [K_b] = \begin{bmatrix} K_{b1} & 0 \\ 0 & K_{b2} \end{bmatrix}, \tag{20a, b}$$

where each sub-matrix can be shown to be precisely,

$$[K_{ll}^*] = \begin{bmatrix} A_1 & \rightarrow \\ \downarrow & K_{ll} \end{bmatrix}, \quad [K_{21}^*] = \begin{bmatrix} 0 & \rightarrow \\ \downarrow & K_{21} \end{bmatrix}, \quad [K_{21}^*] = [K_{12}^*]^{\mathrm{T}}, \tag{21a–c}$$

$$A_l = \left\{\frac{k_{bly}}{R_{ly}^2} \quad 0 \quad 0 \quad 0 \quad -\frac{k_{bly}}{R_{ly}^2} \quad 0\right\}, \tag{21d}$$

$$[K_{bl}] = diag\left[\frac{k_{bly}}{R_{ly}^2} \quad k_{lx} \quad k_{ly} \quad k_{lz} \quad \frac{k_{blx}}{R_{lx}^2} \quad \frac{k_{bly}}{R_{ly}^2} \quad \frac{k_{blz}}{R_{lz}^2}\right]. \tag{21e}$$

Note that k_{li} $(i = x, y, z)$ is the translation stiffness term, and k_{bli} is the related to the effective torsion $(i = y)$ and bending stiffnesses $(i = x, z)$ of the support (bearing) components. For the purpose of applying the forced response analysis by the modal method, the damping matrix $[C_s]$ is assumed to be the proportional viscous type of represent the net vibratory energy dissipation that occurs within the bearing elements and gear mesh interface.

3.3. GENERALIZED EXCITATION AND FORCE COUPLING

The forcing vector on the right-hand side of equation (17) is represented as

$$\{\mathbf{F}(t)\} = \{\mathbf{F}_{int}(t)\} + \{\mathbf{F}_{ext}(t)\} \tag{22a}$$

$$\{\mathbf{F}_{int}(t)\} = \begin{Bmatrix} F_{int}^{(1)} \\ F_{int}^{(2)} \end{Bmatrix}, \quad \{\mathbf{F}_{ext}(t)\} = \begin{Bmatrix} \mathbf{F}_{ext}^{(1)} \\ \mathbf{F}_{ext}^{(2)} \end{Bmatrix}, \tag{22b, c}$$

where forcing sub-vectors $\mathbf{F}_{int}$ and $\mathbf{F}_{ext}$ correspond to the internal load due to the harmonically driven transmission error excitation and the external load fluctuation vector applied to the gear member, motor and output load respectively. They are explicitly given by

$$\mathbf{F}_{int}^{(l)} = \begin{Bmatrix} 0 \\ \sum_{s=1}^{N_c} (k_s h_s^{(l)T} h_s^{(l)}) \mathbf{e}(t) \end{Bmatrix}, \tag{23a}$$

$$\mathbf{F}_s^{(l)} = \{M^{(l)} \;\; F_x^{(l)} \;\; F_y^{(l)} \;\; F_z^{(l)} \;\; M_x^{(l)} \;\; M_y^{(l)} \;\; M_z^{(l)}\}^{\mathrm{T}}, \tag{23b}$$

where the projected transmission error term $\mathbf{e}(t) = \{e_x, e_y, e_z, e_{w_x}, e_{w_y}, e_{w_z}\}^{\mathrm{T}}$ is the vector of equivalent translation and rotation displacements of the pinion relative to the gear resulting from the tooth manufacturing errors and variation of the instantaneous coupling stiffness at the pinion-gear mesh interface. This is generally regarded as the primary excitation source for gear whine by most gear dynamic researchers [9–12]. Here $\mathbf{e}(t)$ can be related back to the classical definition of transmission error along the line of action $\varepsilon(t) = \mathbf{h}_s^{(1)}\mathbf{e}(t)$, where $\varepsilon(t)$ can be obtained by the projection of transmission error given in equation (11) on the line of action. Therefore, it follows that the net generalized dynamic load vector at the gear mesh interface projected onto the centroid of the pinion ($l = 1$) or gear ($l = 2$) can be computed from

$$\mathbf{f}_{mesh}^{(l)}(t) = -[K_{l2}]\mathbf{q}_2 - [K_{l1}]\mathbf{q}_1 + [K_{l1}]\mathbf{e}(t) - [C_{l2}]\dot{\mathbf{q}}_2 - [C_{l1}]\dot{\mathbf{q}}_1 + [C_{l1}]\dot{\mathbf{e}}(t) \tag{24}$$

while the bearing dynamic force vector is predicted using

$$\mathbf{f}_b^{(l)}(t) = -[K_{bl}]\mathbf{q}_l - [C_{bl}]\dot{\mathbf{q}}_l. \tag{25}$$

Since the steady state harmonic response is of primary interest here, the frequency response functions can be computed assuming $\mathbf{q}(t) = \mathbf{q}\exp(\mathrm{i}\omega t)$, where ω is the mesh frequency. The undamped free vibration formulation yields the classical eigenvalue problem $[K]\mathbf{\Phi}_r = \omega_r^2[M]\mathbf{\Phi}_r$, where ω_r is the natural frequency and $\mathbf{\Phi}_r$ is the corresponding modal shape normalized with respect to $[M]$ according to $\Phi_r^{\mathrm{T}}[M]\Phi_r = 1$. The modal damping ratio is $\xi_r = \mathbf{\Phi}_r^{\mathrm{T}}[C_r]\mathbf{\Phi}_r/2\omega_r$. The steady state forced response of the system is directly computed from $Q(\omega) = [H(\omega)]\mathbf{F}(\omega)$, where $\mathbf{Q}(\omega)$ and $\mathbf{F}(\omega)$ are the frequency spectra of $\mathbf{q}(t)$ and $\mathbf{F}(t)$, respectively, and $[H(\omega)]$ is the dynamic compliance matrix derived from the modal superposition method ($\mathrm{i} = \sqrt{-1}$),

$$[H(\omega)] = \sum_{r=2}^{14} \frac{\mathbf{\Phi}_r\mathbf{\Phi}_r^{\mathrm{T}}}{(\omega_r^2 - \omega^2 + 2\mathrm{i}\xi_r\omega\omega_r)} = \begin{bmatrix} H_{11} & H_{12} \\ H_{21} & H_{22} \end{bmatrix}. \tag{26}$$

In the forced response analysis, the mesh force vector $f_{mesh}^{(l)}$ in equation (24) can be used to determine the severity of gear tooth loading and vibration transmissibility. The modal frequency response functions computed using equation (26) is used to transform the time-dependent mesh force vector into the spectral domain by applying the Fourier transform as

$$F_{mess}^{(l)}(\omega) = -[K_{l2}]Q_2(\omega) - [K_{ll}]Q_l(\omega) + [K_{l1}]E(\omega) - [C_{l2}]\dot{Q}_2(\omega) - [C_{ll}]\dot{Q}_l(\omega) + [C_{l1}]\dot{E}(\omega), \tag{27a}$$

$$\begin{Bmatrix} Q_1(\omega) \\ Q_2(\omega) \end{Bmatrix} = \{H\}\cdot\begin{Bmatrix} F_1(\omega) \\ F_2(\omega) \end{Bmatrix} = \begin{bmatrix} H_{11} & H_{12} \\ H_{21} & H_{22} \end{bmatrix}\begin{bmatrix} K_{11}E(\omega) + F_{ext}^{(1)}(\omega) + \mathrm{i}\cdot C_{11}\dot{E}(\omega) \\ K_{21}E(\omega) + F_{ext}^{(2)}(\omega) + \mathrm{i}\cdot C_{21}\dot{E}(\omega) \end{bmatrix}, \tag{27b}$$

where $\mathbf{Q}(\omega)$ and $\mathbf{E}(\omega)$ are the complex-valued, Fourier transforms of $\mathbf{q}(t)$ and $\mathbf{e}(t)$, respectively, and $F_l(\omega)$ is the spectral function of $F_{ext}^{(l)}(t)$. Direct substitution of

equation (27b) into (27a) gives

$$\mathbf{F}^{(l)}_{mesh}(\omega) = [G^{(l)}(\omega)]\mathbf{E}(\omega) + [R^{(l)}(\omega)]\mathbf{F}^{(1)}_{ext}(\omega) + [R^{(l2)}(\omega)]\mathbf{F}^{(2)}_{ext}(\omega), \tag{28a}$$

$$[R^{(l1)}(\omega)] = [D_{l1}][H_{11}] + [D_{l2}][H_{21}], \tag{28b}$$

$$[R^{(l1)}(\omega)] = [D_{l1}][H_{12}] + [D_{l2}][H_{22}], \tag{28c}$$

$$[D_{ij}(\omega)] = [K_{ij}] + \mathrm{i}\omega[C_{ij}] \quad (i, j = 1, 2), \tag{28d}$$

$$[G^{(l)}(\omega)] = [D_{l1}] - ([D_{l1}][H_{11}] + [D_{l2}][H_{21}])[D_{l1}] - ([D_{l1}]([H_{12}] + ([D_{l2}][H_{22}])[D_{21}], \tag{28e}$$

where $[G^{(l)}(\omega)]$ is the mesh-related dynamic stiffness transfer function matrix of dimension six similar to that derived by Blankenship and Singh [11] for parallel axis gears. This matrix $[G^{(l)}(\omega)]$ physically describes the dynamic load vector generated within the gear mesh interface due to $\mathbf{e}(t)$, which directly acts on the pinion ($l = 1$) or gear ($l = 2$) body centers of mass. On the other hand, $[R^{(l1)}(\omega)]$ and $[R^{(l2)}(\omega)]$ are the transmissibility transfer function matrices for the dynamic load reaction vector due to the external load fluctuations acting on the pinion ($l = 1$) and gear ($l = 2$), respectively, via the gear mesh interface, and $[D_{ij}(\omega)]$ is the complex-valued mesh stiffness matrix. Similarly, the dynamic load reaction vector of the pinion bearing supports in the frequency domain form can also be obtained using the same derivation technique, resulting in

$$F^{(l)}_b(\omega) = [G^{(l)}_b(\omega)]E(\omega) + [R^{(1)}_b(\omega)]F^{(1)}_{ext} + [R^{(2)}_b(\omega)]F^{(2)}_{ext}, \tag{29a}$$

$$[G^{(1)}_b(\omega)] = -[D_{bl}]([H_{l1}][D_{11}] + [H_{l2}][D_{21}]), \tag{29b}$$

$$[R^{(l)}_b(\omega)] = -[D_b][H_{l1}], \quad [D_{bl}(\omega)] = [K_{bl}] + \mathrm{i}\omega[C_{bl}], \tag{29c, d}$$

where $\mathbf{F}^{(l)}_b(\omega)$ is the complex-valued Fourier transform of $\mathbf{f}^{(l)}_b(t)$, and $[G^{(l)}_b(\omega)]$ refers to the dynamic reaction forces and moments acting on the pinion ($l = 1$) or gear ($l = 2$) support bearing due to harmonically driven unit magnitude of $\mathbf{e}(t)$. Also, $[\mathbf{R}^{(l)}_b]$ in the above expressions characterizes the transmissibility of the external harmonic load fluctuation vectors acting on the driving pinion $\mathbf{F}^{(1)}_{ext}$ and driven gear $\mathbf{F}^{(2)}_{ext}$ to the support bearing reaction load vectors for the pinion ($l = 1$) via the gear mesh interface.

Suppose the contact cells encompass centrally around the effective pitch point position that is definable by the theoretical surface normal vector, the effective mesh stiffness can be derived without loss of generality as

$$\sum_{s=1}^{N_c} k_s \mathbf{h}^{(l)^{\mathrm{T}}}_s \mathbf{h}^{(l)}_s \cong K_m \mathbf{h}^{(l)^{\mathrm{T}}} \mathbf{h}^{(l)}, \quad \sum_{s=1}^{N_c} k_s \mathbf{h}^{(l)^{\mathrm{T}}}_s \mathbf{h}^{(l)}_s \mathbf{e}(t) \cong K_m \mathbf{h}^{(l)^{\mathrm{T}}} \mathbf{h}^{(l)}\, \mathbf{e}(t), \tag{30a, b}$$

where K_m is the spatially averaged mesh stiffness and assumed to be a constant in the following analysis. Also, since we are primarily interested in the perturbations above the mean steady state operating condition, it is assumed that the external forcing vector $\mathbf{F}_{ext}(t) = \{0\}$, and the internal forcing vector $\mathbf{F}_{int}(t)$ is solely due to $\mathbf{e}(t)$. The resultant dynamic model is still relatively general and can be applied to predict dynamic transmission error, mesh force, and bearing reaction forces for a variety of steady state operating conditions, such as forward drive and coast conditions. The proposed theory can also

account directly for the effects of variations in the hypoid gear parameters, such as pinion offset and pinion mean spiral angle, which also induce changes in other gear design parameters such as pitch angles and pressure angles of both convex and concave sides of the gear teeth, on system vibration response. To the knowledge of the authors, this type of model has never been proposed in the past.

Accordingly, the corresponding dynamic transmission error that quantifies the effect of tooth deflection along the effective line-of-action due to vibratory motion of gear bodies is given by $\delta_d(t) = \mathbf{h}^{(2)}\mathbf{q}_2 - \mathbf{h}^{(1)}\mathbf{q}_1$. Furthermore, the scalar dynamic mesh force along the line-of-action is expressed as

$$F_\delta(t) = K_m(\delta_d(t)(+ \varepsilon(t)) + C_m(\dot{\delta}_d(t) + \dot{\varepsilon}(t)). \tag{31}$$

Note that the magnitude of F_δ generally plays a major role in determining the sensitivity of a transmission design to gear noise, and is frequently used as a design metric. Such a design concept has been applied in previous studies on spur and helical gears [10,11,20,30,31] and is being extended to the hypoid case here. In addition, the dynamic bearing reaction loads are of interest here because they represent the vibratory energy that is transmitted into the housing and surrounding structure, and is often directly proportional to the radiated gear-noise levels.

4. NUMERICAL RESULTS

4.1. MODAL PROPERTIES

A baseline automotive hypoid gear set that is defined in Tables 1 and 3 is used in the subsequent dynamic analysis. First, the eigensolution corresponding to the free vibration problem is used to identify the critical elastic modes that directly affect gear-mesh force and thus gear noise. Since the severity of the system dynamic response is directly associated with the amplitude of the mesh displacement vector, a *modal index* $\mathbf{T}_r = \mathbf{\Phi}_r^{\mathrm{T}}[\{0, \mathbf{h}^{(1)}\}\ \{0, \mathbf{h}^{(2)}\}]^{\mathrm{T}}$ is defined to account for the relative modal shape projection along the mesh direction. Hence, ts magnitude can be used to differentiate the modes that affect dynamic response significantly. The predicted $\mathbf{T}_r$ values corresponding to the critical out-of-phase gear pair torsional modes that are classically most susceptible to the excitation of $\mathbf{e}(t)$ for the baseline

TABLE 3

Baseline system parameters for a typical automotive hypoid gear set (left-hand pinion)

Mass moment of inertia of the driver (kg m^2)	0·0055	Mass moment of inertia of the pinion (kg m^2)	0·0083
Mass moment of inertia of the load (kg m^2)	0·1	Mass moment of inertia of the gear (kg m^2)	0·5233
Mass of the pinion (kg)	11·48	Mass of the gear (kg)	49·53
Torsional stiffness of shafts (Nm/rad)	1·0E4 (pinion) 5·0E5 (gear)	Shaft-bearing bending stiffness (Nm/rad)	1·0E6 (pinion) 8·0E6 (gear)
Axial support stiffness (N/m)	1·0E8	Lateral support stiffness (N/m)	3·8E8
Mesh stiffness (N/m)	6·0E8	Mean torque (in lbf)	12 000

TABLE 4

Modal indices for the critical class of out-of-phase torsion gear pair modes

Mode number, r	T_r	ω_r (Hz)	Mode description
2	0·013	206·3	Out-of-phase torsion, pinion and gear axial translation
4	0·021	351·8	Out-of-phase torsion, pinion axial translation and gear transverse motion
8	0·084	799·8	Out-of-phase torsion, gear yaw motion, and pinion axial and vertical translation
12	0·367	1419·7	Out-of-phase torsion, pinion yaw motion, and pinion axial and vertical translations
14	1·000	3120·8	Out-of-phase torsion, pinion yaw motion

system are given in Table 4. Here, $\mathbf{T}_r$ is normalized in such a manner as to ensure a maximum level of unit within the same modal set. An illustration of this class of critical modes is given in Figure 4. The result shows that $T_r = 0{\cdot}1$ corresponds to the out-of-phase gear pair torsional mode with a superimposed pinion yaw motion. Thus, this mode is expected to be very sensitive to $\mathbf{e}(t)$. A complementary technique for analyzing the severity and nature of the vibration modes can also be applied here, which relies on the computation of the modal strain energy ratio of each elastic element in the geared rotor system model. Using this technique, the critical structural components that contribute to the mode in question may be identified. Figure 5 shows the distribution of modal strain energy ratio of the five dominant out-of-phase gear pair torsion modes. The translation or torsion compliances tend to affect the lower modes, while the bending stiffness controls the higher order ones. Also, the structural modes possessing a higher percentage of mesh strain energy density actually generate higher response peaks, which will be evident from the response spectra presented in the next section. It is also observed that the specific modes with larger T_r values possess generally higher mesh strain energy ratio, and hence further validating the correlation between $\mathbf{T}_r$ and the effectiveness of the modal mesh in storing vibratory energy.

4.2. MESH LOAD TRANSMISSIBILITY

Previous studies of hypoid gear dynamics ignored the effect of bending load transmissibility and included only torsion component [13,18,19]. The present theory that incorporates the dynamic mesh force transfer function matrices, given by $[G^{(l)}(\omega)]$, $[R^{(l1)}(\omega)]$ and $[R^{(l2)}(\omega)]$, in the gear mesh reaction load vector formulation provides a direct means to examine these effects more thoroughly. In this analysis, $[G^{(l)}(\omega)]$ is a symmetric matrix of dimension six with 21 distinct terms where each element $G^{(l)}_{q_i q_j}$ represents the q_ith component of the dynamic load vector related to the mesh coupling acting on the pinion ($l = 1$) or gear ($l = 2$) due to the q_jth component of projected transmission error excitation. On the other hand, $[R^{(lk)}(\omega)]$ is a non-symmetric matrix of dimension six with 36 distinct terms. Each term denoted by $R^{(lk)}_{q_i q_j}$ defines the q_ith component of mesh related dynamic load vector acting on the pinion ($l = 1$) or gear ($l = 2$) due to the q_jth component of external load fluctuation on the pinion ($k = 1$) or gear ($k = 2$). Also note that the subscripts q_i and q_j can take the value of x, y, z, w_x, w_y and w_z. Figure 6 shows the frequency response functions of the pinion lateral shear, axial force, bending moment and torque response components of

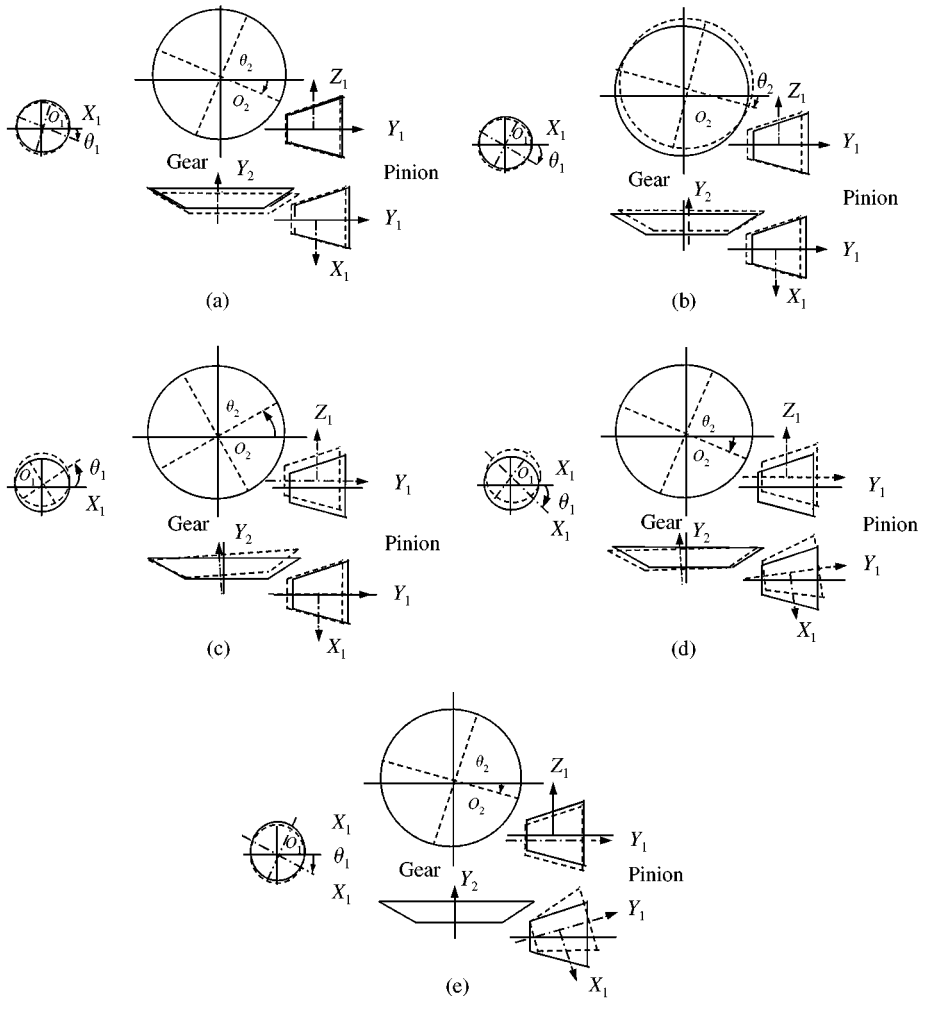

Figure 4. Critical class of out-of-phase gear pair torsional mode shapes: (——), original position; (– – –), deflected position; (a) mode 2; (b) mode 4; (c) mode 8: (d) mode 12; and (d) mode 14.

$[G^{(1)}(\omega)]$ per unit torsion component of transmission error excitation. It may be noted that the elemental functions of $[G^{(1)}(\omega)]$ not shown here are also comparable in magnitude with the similar spectral content that arises from the contributions of the critical modes described in Figure 4. The relative amplitudes of these resonance peaks in fact correlate extremely well with the results of T_r. In addition, the cross coupling terms of $[G^{(1)}(\omega)]$ are nearly as significant if not more than its diagonal terms. This implies that all six components of projected transmission error excitation contribute strongly to the dynamic response of the system, and the analysis actually proves that the hypoid gear dynamic problem must be treated by the inclusion of a complete 3D 6 d.o.f. representation of the gear body. In contrast, the simplified mesh force vector used in the previous studies [13,17–19] can only be used to account for $G^{(l)}_{z-w_y}(\omega)$, $G^{(l)}_{w_x-w_y}(\omega)$ and the diagonal terms $G^{(l)}_{q_i q_i}(\omega)$. Hence, the mesh force transmissibility calculations are limited to simply the vertical translation z, torsion w_y and bending w_x co-ordinates, and the equally critical lateral x, axial y and beding w_z components cannot be predicted.

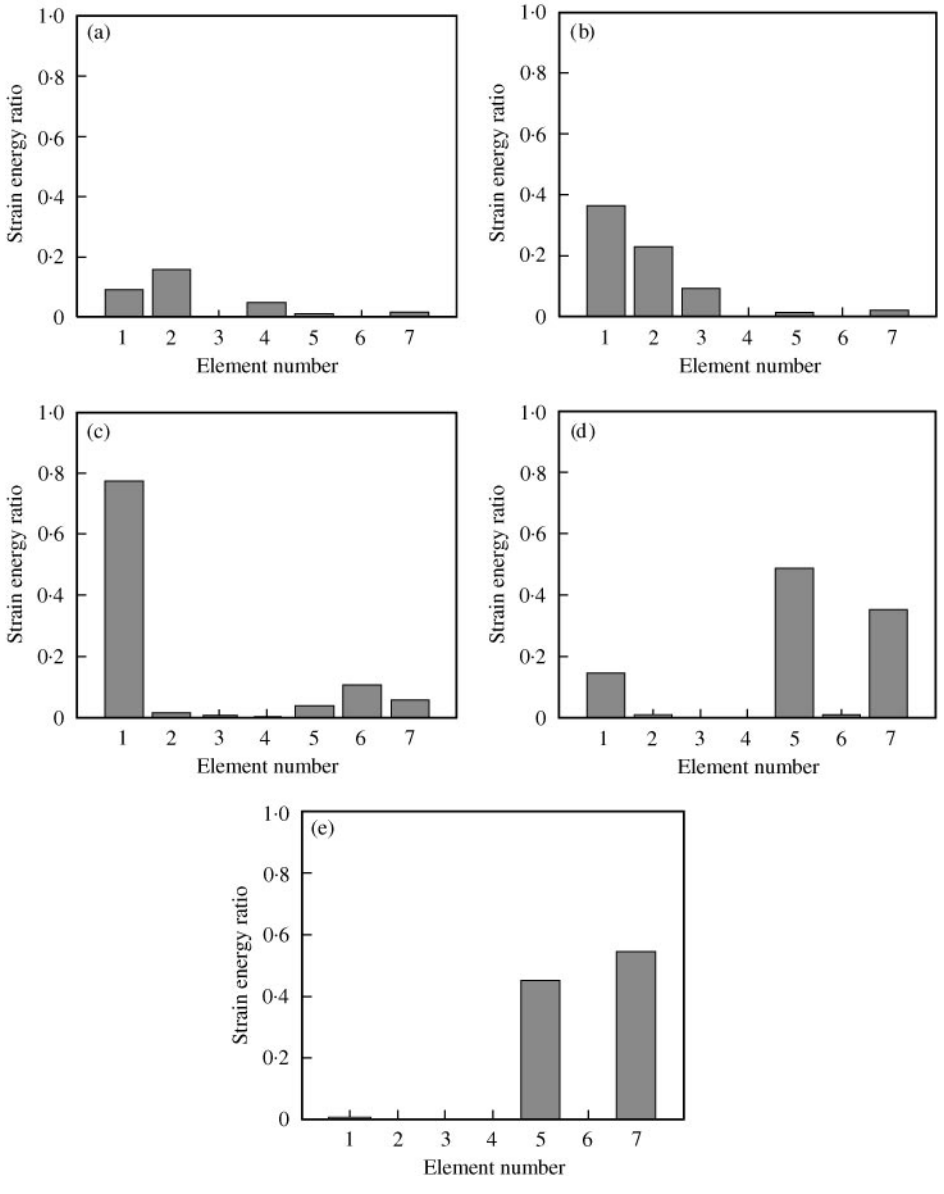

Figure 5. Modal strain energy distributions for the five critical baseline system modes. (1, 2; pinion and gear translation compliances; 3, 4; pinion and gear rotational compliances; 5, 6; pinion and gear bending compliances; 7; mesh compliances); (a) 206·3 Hz; (b) 351·8 Hz; (c) 799·8 Hz; (d) 1419·7 Hz; (e) 3120·8 Hz.

Figures 7 and 8 show the force and moment transmissibility functions of $R_{jq_i}^{(l)}$ and $R_{w_i q_i}^{(l1)}$ ($j = x, y, z$) respectively. The former type of functions is essentially associated with the translation mesh force components acting on the pinion center of mass, while the latter set of terms is related to the rotational ones. By comparing the transfer function in Figures 7 and 8, it can be seen that the torque excitation corresponding to the w_y co-ordinate frequently produces the highest resonant peaks compared to the other excitations due to coupling provided by the gear mesh. Also, the axial mesh force component is more sensitive to external axial force and torque fluctuations compared to the pitching-type external

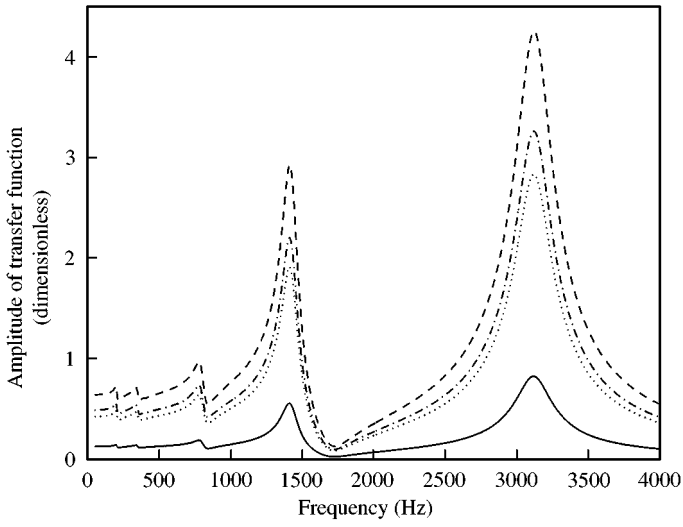

Figure 6. Mesh related pinion dynamic load transfer function with the amplitude normalized to the mean mesh stiffness. ———, $G^{(1)}_{x-w_y}$; – · – · –, $G^{(1)}_{y-w_y}$; – – – – –, $G^{(1)}_{w_x-w_y}$; ·····, $G^{(1)}_{w_y-w_y}$.)

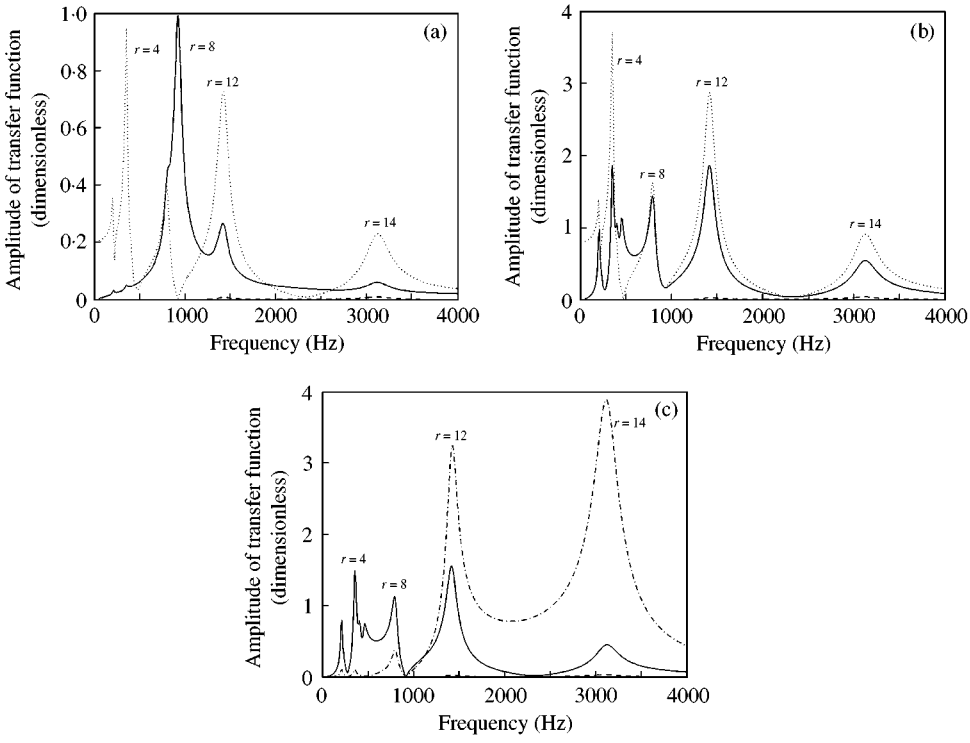

Figure 7. Frequency response functions of $[R^{(11)}(\omega)]$ corresponding to the translational components of mesh force vector acting on the pinion center of mass due to external driving load fluctuations: (a) ———, $R^{(11)}_{x-x}$; – – – –, $R^{(11)}_{x-w_x}$; ·····, $R^{(11)}_{x-w_y}$; (b) ———, $R^{(11)}_{y-y}$; – – – –, $R^{(11)}_{y-w_x}$; ·····, $R^{(11)}_{y-w_y}$; (c) ———, $R^{(11)}_{z-y}$; – – – –, $R^{(11)}_{z-w_x}$; ·····, $R^{(11)}_{z-w_z}$

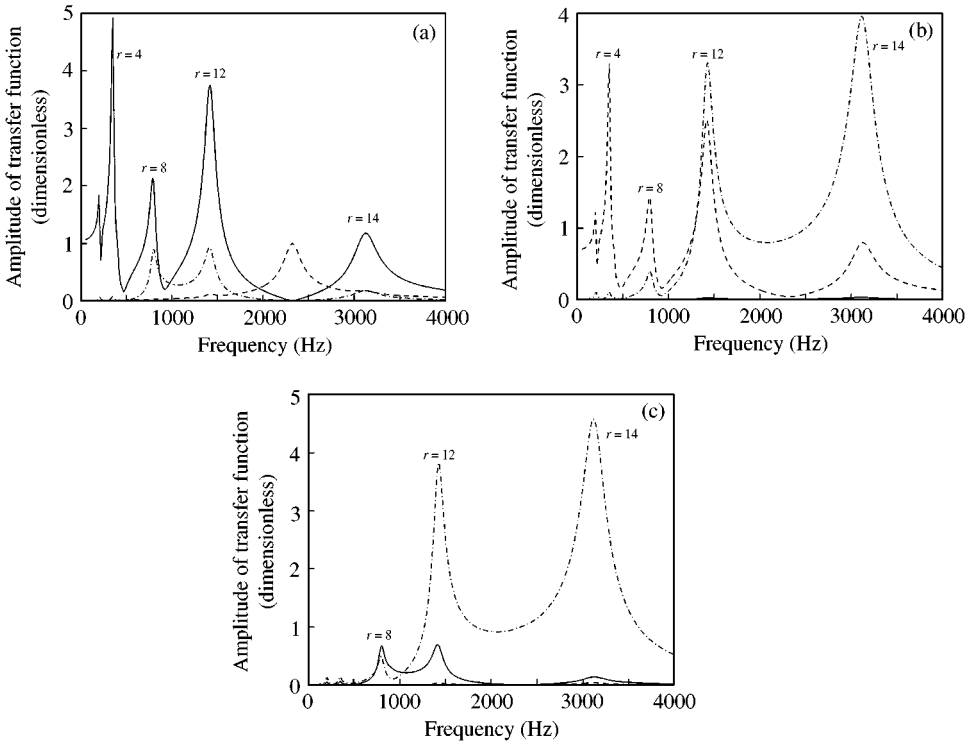

Figure 8. Frequency response functions of $[R^{(11)}(\omega)]$ corresponding to the rotational components of mesh force vector acting on the pinion center of mass due to external driving load fluctuations: (a) – · – · –, $R^{(11)}_{w_x-x}$; – – –, $R^{(11)}_{w_x-w_x}$; ———, $R^{(11)}_{w_x-w_y}$; (b) ———, $R^{(11)}_{w_y-w_z}$; – – –, $R^{(11)}_{w_y-w_y}$; – · – · –, $R^{(11)}_{w_y-w_z}$; (c) ———, $R^{(11)}_{w_z-x}$; – – –, $R^{(11)}_{w_z-w_z}$; – · – · –, $R^{(11)}_{w_z-w_z}$.

bending moment associated with the w_x co-ordinate as seen in Figure 7. In fact, the external bending moment is observed to be nearly uncoupled from many of its other co-ordinate counterpart. This is evidenced from its small effect on the pinion bending moment $R^{(11)}_{\theta_z-\theta_x}$ and reaction torque $R^{(11)}_{\theta_y-\theta_x}$ in Figure 8, and on the translation force components of the mesh reaction force vector $R^{(11)}_{u-\theta_z}$ in Figure 7. It is also noticed that the vertical mesh force response is more sensitive to the pinion yaw-type bending moment excitation corresponding to the θ_z co-ordinate as characterized by $R^{(11)}_{z-\theta_z}$, at high frequency, in Figure 7(c). Furthermore, the external drive torque fluctuation about the Y-axis affects the low-frequency resonance $r = 4$ significantly as depicted by $R^{(11)}_{q_i-\theta_y}$ in Figures 7 and 8, while the bending moment about the Z-axis affects the high-frequency modes such as mode 14. Meanwhile, other external load fluctuations with the exception of the bending moment about the X-axis also contribute significantly to the response from mid-frequency modes 8 and 12.

4.3. PARAMETRIC ANALYSIS

The effect of pinion spiral angle β_1 on the dynamic response solely due to transmission error excitation $\varepsilon(t)$ will be investigated next to demonstrate the effectiveness of the proposed model for use in parametric design studies. Pinion spiral angle directly affects the direction of the mesh force coupling vector and contact position, and thus the structure

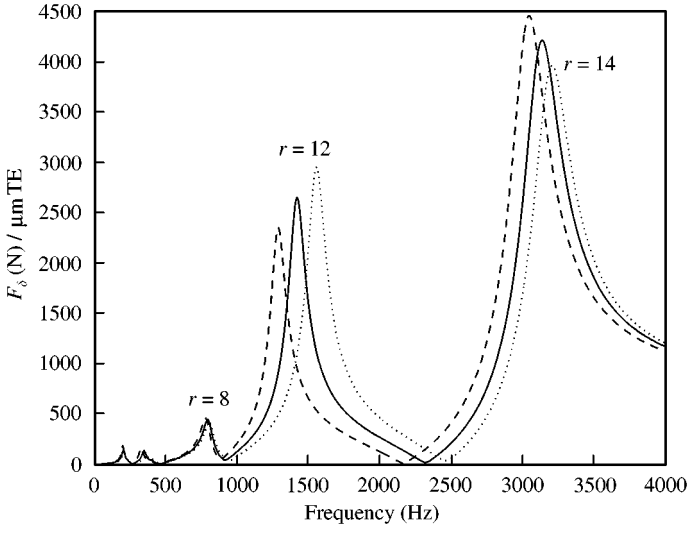

Figure 9. Effect of pinion spiral angle β_1 on net dynamic mesh force response along the line of action per μm TE: (·····, 41°; ———, 46°; – – – –, 51°).

stiffness matrix $[K]$ of the system. Note that varying the spiral angle also requires re-computation of other gear parameters, such as the gear spiral angle β_2, pitch angles and pressure angle.

The effect of β_1 on the amplitude of the dynamic mesh force along the line of action F_δ defined by equation (31) is shown in Figure 9. Generally, we see a uniform softening of the system modes with increasing β_1 primarily due to incremental reduction in the mesh coupling strength. As a result, the critical modes were lowered by approximately 10%/5° increase in β_1. The spectral results also show an opposing frequency-dependent effect on the two most critical modes. For mode 12 in the vicinity of 1400 Hz, the amplitude response reduces with increasing β_1. On the other hand, the higher mode 14 near 3100 Hz actually becomes more sensitive to higher β_1. This behavior is typical of a geared rotor dynamic system possessing frequency ranges with high and low sensitivities to transmission error excitation, which is also observed in spur and helical gear cases [32].

The effect of β_1 on bearing force transmissibility can be predicted as well. Figure 10 shows the harmonic component of the pinion-bearing reaction force in the axial direction. In this case, we see a systematic increase in this component of bearing force over a broad frequency range due to either an increase in F_δ or coupling between the line of action and axial co-ordinate. It is worthwhile to note that the previous simplified mesh models are unable to predict this axial or the lateral bearing reaction load accurately, which can be just as critical to the structure-borne gear noise transmissibility in the system.

Thirdly, Figures 11 and 12 illustrate the effect of β_1 on selected two transfer functions of $[G^{(1)}(\omega)]$. The transfer function $G^{(1)}_{x-w_y}(\omega)$ for the lateral component of mesh force vector acting on the pinion centroid due to the torsion element of the projected transmission error excitation is given by Figure 11. Its result shows a frequency-wide uniform reduction in amplitude primarily due to lower coordinate coupling as the spiral angle is increased. The other transfer function $G^{(1)}_{y-w_y}(\omega)$ corresponding to the axial component of mesh force on the pinion depicts a trend similar to F_δ shown in Figure 12, as expected. These results illustrate the feasibility of applying the proposed theory in predicting dynamic response associated with the complete 6 d.o.f. co-ordinate of the hypoid geared rotor system, and the potential of

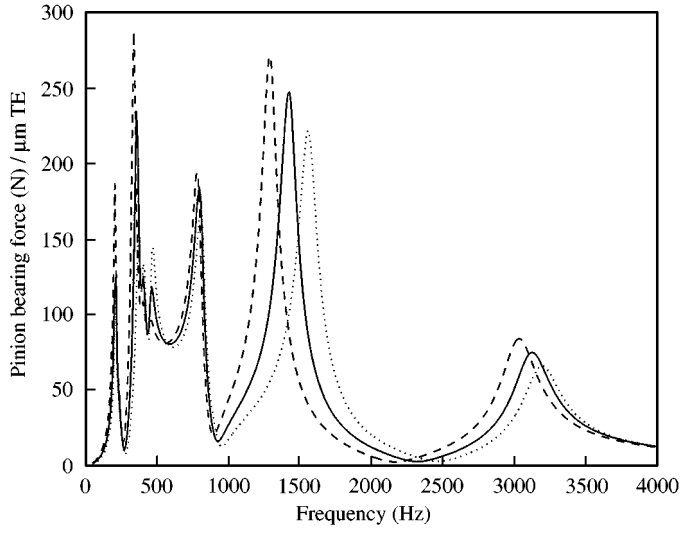

Figure 10. Effect of pinion spiral angle β_1 on pinion axial bearing force due to a unit magnitude of transmission error excitation. (·····, 41°; ———, 46°; – – – –, 51°).

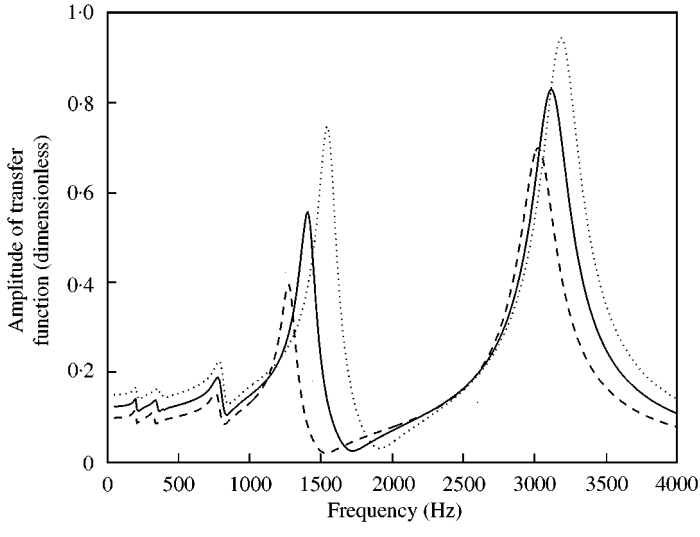

Figure 11. Effect of pinion spiral angle β_1 on $G^{(1)}_{x-w_y}$ (·····, 41°; ———, 46°; – – – –, 51°).

tuning fundamental hypoid gear design parameters to a lower undesirable and sometimes harmful vibration response for a targeted frequency range.

Finally, the present formulation can also be used to study the experimental phenomenon observed by Nakayashiki *et al.* [17], where the dynamic response of the forward drive and coast operating conditions are found to be different due to the effect of change in the gear tooth engagement side. Figure 13 illustrates the predicted differences in the dynamic mesh force spectra of the forward drive and coast operating conditions for the baseline system defined in Table 3, which turns out to be quite similar to the experimental observation. The analysis shows that the drive operating condition actually produces a higher amplitude of

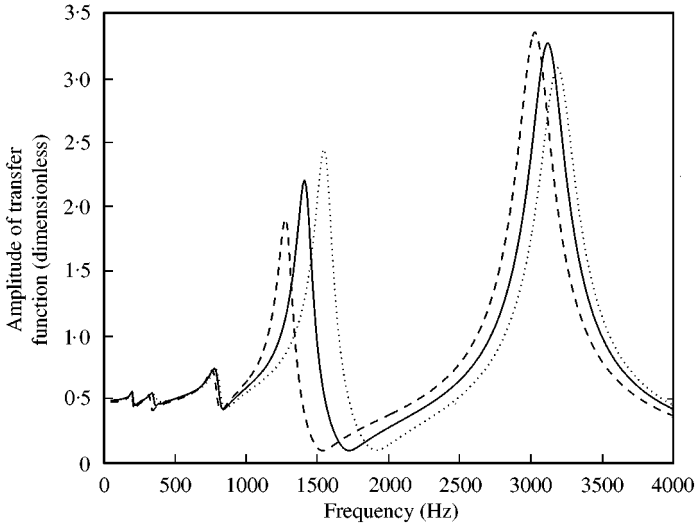

Figure 12. Effect of pinion spiral angle β_1 on $G^{(1)}_{y-w_x}$ (·····, 41°; ———, 46°; – – – –, 51°).

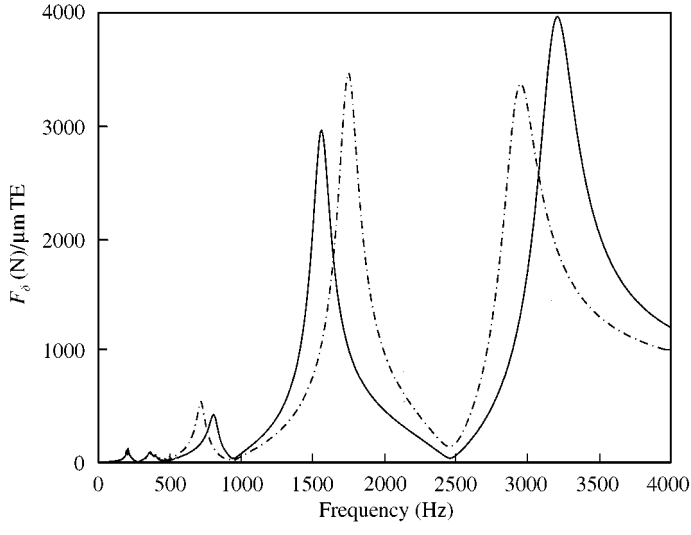

Figure 13. Total mesh force spectra of the forward drive and coast operating condition. (———, drive; – · – · – ·, coast.)

peak response for the highest resonance frequency shown, but lower levels for other resonance frequencies when compared with the response of the coast condition. These variations are primarily due to the differences in the gear mesh coupling characteristics that cause the alterations in the resultant system stiffness matrix. This is clearly unpredictable by the simpler gear mesh formulation described earlier.

5. CONCLUDING REMARKS

A new gear mesh coupling formulation is developed based on the exact gear geometry and kinematic relations that are derivable from the manufacturing parameters. This new

theory is incorporated into a 3D multiple-d.o.f.s dynamic model of the hypoid gear pair. Free and forced vibrations in the presence of transmission error excitation are examined, and the critical class of pinion-gear out-of-phase torsion modes that affect the undesirable vibration response are identified. The proposed system model also readily provides the complete gear mesh transfer functions and force transmissibility spectra, which is used to characterize the nature of the system vibratory behavior including the dynamic coupling and sensitivity of the vibratory response to critical design parameters. Our analysis suggests that all 6 d.o.f.s representations of the gear bodies must be included in the dynamic model to accurately account for the response due to the transmission error excitation and external load fluctuations. The results also show new mesh coupling effect from lateral, axial, and bending co-ordinates, which was not modelled in the simpler gear mesh representations utilized in the previous studies. Numerous parametric studies are performed to quantify the dependence of dynamic characteristics and vibration response to basic gear design parameters and operating conditions, and explain the difference in the dynamic response of forward drive versus coast conditions. It may be noted that even though our analysis is based on the time-invariant assumption, the gear-mesh-coupling theory is also applicable to time-varying modelling, which is the focus of our next research activity.

REFERENCES

1. F. L. Litvin and Y. Gutman 1981 *Journal of Mechanical Design* **103**, 83–113. Method of synthesis and analysis for hypoid gear-drives of format and helixform.
2. C Gosselin, L. Cloutier and S. Sankar 1989 *Proceedings of the* 1989 *International Power Transmission Gearing Conference*: *New Technologies for Power Transmissions of the* 90's, *Chicago, IL*, 705–712. Effects of the mechine settings on the transmission error of spiral bevel gears cut by the gleason method.
3. M. Sugimoto, N. Maruyama, A. Naruyama and M. Hitomi 1991 *Journal of Mechanical Design*, *Transaction of American Society of Mechanical Engineers* **113**, 182–187. Effects of tooth contact and gear dimensions on transmission errors of loaded hypoid gears.
4. K. Takahashi and N. Ito 1986 *Journal of Mechanics*, *Transmission and Automation in Design Transactions of American Society of Mechanical Engineers*, **108**, 263–269. Third-order surface application to determine the tooth contact pattern of hypoid gears.
5. T. J. Krenzer 1981 *SAE Paper* 810688. Tooth contact analysis of spiral bevel and hypoid gears under load.
6. Gleason Works, 1981 *Gleason Works Publication SD* 3139*B*, *January* 1981. Understanding tooth contact analysis.
7. S. Tilak 1990 *M.Sc. Thesis*, *The Ohio State University*, *Columbus*, *OH*. *Design*, Analysis and inspection of spiral bevel and hypoid gears using tooth contact analysis programs.
8. Y. Lin, C. B. Tsay and Z. H. Fong 1997 *Mechanics and Machins Theory* **32**, 121–136. Mathematical model of spiral bevel and hypoid gears manufactured by the modified roll method.
9. H. N. Özgüven and D. R. Houser 1988 *Journal of Sound and Vibration* **121**, 383–411. Mathematical models used in gear dynamic—A review.
10. A. Kahraman and R. Singh 1990 *Journal of Sound and Vibration* **142**, 49–75. Non-linear dynamics of a spur gear pair.
11. G. W. Blankenship and R. Singh 1995 *Mechanics Machins Theory* **30**, 323–339. Dynamic force transmissibility in helical gear pairs.
12. P. Velex and M. Maatar 1996 *Journal of Sound and Vibration* **191**, 629–660. A mathematical model for analyzing the influence of shape deviations and mounting errors on gear dynamic behavior.
13. E. P. Remmers 1971 *SAE Paper* 710114. Dynamics of automotive rear axle gear noise.
14. S. Kiyono, Y. Fujii and Y. Suzuki 1981 *Bulletins of JSME* **24**, 441–446. Analysis of vibration of bevel gears.
15. Y. Terauchi and Y. Miyao, M. Fujii and K. Sagawa 1980 *Bulletin JSME* **1980**, 126–131. Dynamic behavior of straight bevel gears (1st report: dynamic load, torque variation and bending vibration of gear shaft.

16. Z. D. FANG, 1994 *Proceedings of* 1994 *International Gearing Conference*, Newcastle, 389–392. Dynamic analysis of spiral bevel gears in assembly.
17. A. NAKAYASHIKI, K. KUBO and H. IMANISHI 1983 *Proceedings—Society of Automotive Engineers* P-139 2. 571–580. Tokyo, Japan: Published by JSAE. One approach on the axle gear noise generated from the torsional vibration.
18. E. ABE and H. HAGIWARA 1990 *Gear Design, Manufacturing and Inspection Manual,* 223–236. Warrendale, PA: Society of Automotive Engineers. Advanced method for reduction in axle gear noise.
19. N. HIRASAKA, H. SUGITA and M. ASAI 1991 *Journal of Passenger Cars* **100**, 1383–1387. A simulation method of rear axle gear noise.
20. M. G. DONLEY, T. C. LIM and G. C. STEYER 1992 *Journal of Passenger Cars* **101**, 77–87. Dynamic analysis of automotive gearing systems.
21. S. VIJAYAKAR 1987 *Ph.D Dissertation*, *The Ohio State University*, *Columbus*, *OH*. Finite element methods for quasi-prismatic bodies with application to gears.
22. C. GOSSELIN, L. CLOUTIER and Q. D. NGUYEN 1995 *Mechanics and Machines Theory* **30**, 433–450. A general formulation for the calculation of the load sharing and transmission error under load of spiral bevel and hypoid gears.
23. M. L. BAXTER 1961 *Industrial Mathematics* **11**, 19–43. Basic geometry and tooth contact of hypoid gears.
24. Gleason Works 1971 *Gleason Works Publication SD* 3030D. Methods for designing hypoid gear blanks.
25. A. SHTIPELMAN 1987 *Design and Manufacture of Hypoid Gears.* New York: Wiley-Interscience Publication.
26. T. C. LIM and Y. CHENG 1999 *Journal of Mechanical Design*, *Transactions of American Society of Mechanical Engineers* **121**, 594–601. A theoretical study of the effect of pinion offset on the dynamics of hypoid geared rotor system.
27. F. L. LITVIN 1989 *Theory of Gearing*, *NASA Reference Publication* 1212.
28. F. L. LITVIN, W. S. CHAING, M. LUNDY and W. J. TSUNG 1990 *Journal of Mechanical Design* **112**, 413–418. Design of pitch cones for face-hobbed hypoid gears.
29. T. C. LIM and R. SINGH 1990 *Journal of Sound and Vibration* **139**, 179–199. Vibration transmission through rolling element bearing. Part 1: bearing stiffness formulation.
30. H. N. ÖZGÜVEN and D. R. HOUSER 1988 *Journal of Sound and Vibration*, **125**, 71–83. Dynamic analysis of high speed gears by using loaded static transmission error.
31. J. RAUTERT and F. G. KOLLMANN 1989 *Proceedings of* 1989 *International Power Transmission. Gearing Conference*: *New Technologies for Power Transmissions of the* 90's, *Chicago*, *IL*, 435–446. Computer simulation of dynamic forces in helical and bevel gears.
32. A. KAHRAMAN, 1993 *ASME Journal of Vibration and Acoustics* **115**, 33–39. Effect of axial vibrations on the dynamics of a helical gear pair.

APPENDIX A: TOOTH CONTACT SIMULATION MATRICES

$$\mathbf{r}_1^{(1)}(u_1, v_1, \phi_c) = [M_{w1t1}(v_1, \phi_c)\mathbf{r}_{t1}^{(1)}(u_1) = [M_{w1p}][M_{pn}][M_{nm1}][M_{m1c}][M_{cb}][M_{bt1}]\mathbf{r}_{t1}^{(1)}, \tag{A1}$$

$$\mathbf{n}_1^{(1)}(u_1, v_1, \phi_c) = [M_{w1t1}(v_1, \phi_c)]\mathbf{n}_{t1}^{(1)}(u_1) = [M_{w1p}][M_{pn}][M_{nm1}][M_{m1c}][M_{cb}][M_{bt1}]\mathbf{n}_{t1}^{(1)}, \tag{A2}$$

$$\mathbf{r}_f^{(1)} = [M_{f1}]\mathbf{r}_{w1}^{(1)} = \mathbf{r}_f^{(1)}(u_1, v_1, \phi_c, \phi_1'), \quad \mathbf{n}_f^{(1)} = [M_{f1}]\mathbf{n}_{w1}^{(1)} = \mathbf{n}_f^{(1)}(u_1, v_1, \phi_c, \phi_1'), \tag{A3, 4}$$

$$\mathbf{r}_{t1}^{(1)}(u_1, v_1) = \begin{bmatrix} (r_{cP} + u_1 \sin\phi_{BP})\cos v_1 \\ (r_{cP} + u_1 \sin\phi_{BP})\sin v_1 \\ -u_1 \cos\phi_{BP} \\ 1 \end{bmatrix}, \quad \mathbf{n}_{t1}^{(1)}(u_1, v_1) = \begin{bmatrix} \cos\phi_{BP}\cos v_1 \\ \cos\phi_{BP}\sin v_1 \\ \sin v_1 \\ 0 \end{bmatrix}, \tag{A5, 6}$$

$$[M_{bt1}] = \begin{bmatrix} \cos(i_c) & 0 & \sin(i_c) & 0 \\ 0 & 1 & 0 & 0 \\ -\sin(i_c) & 0 & \cos(i_c) & 0 \\ 0 & 0 & 0 & 1 \end{bmatrix}, \tag{A7}$$

$$[M_{cb}] = \begin{bmatrix} -\sin(J_c \mp Q_c) & \mp\cos(J_c \mp Q_c) & 0 & S_R\cos(Q_c) \\ \pm\cos(J_c \mp Q_c) & -\sin(J_c \mp Q_c) & 0 & -S_R\sin(Q_c) \\ 0 & 0 & 1 & 0 \\ 0 & 0 & 0 & 1 \end{bmatrix}, \tag{A8}$$

The upper and lower signs in equation (A8) imply the left- and right-hand pinion respectively:

$$[M_{m1c}] = \begin{bmatrix} \cos\phi_c & \sin\phi_c & 0 & 0 \\ -\sin\phi_c & \cos\phi_c & 0 & 0 \\ 0 & 0 & 1 & 0 \\ 0 & 0 & 0 & 1 \end{bmatrix}, \quad [M_{nm1}] = \begin{bmatrix} 1 & 0 & 0 & 0 \\ 0 & 1 & 0 & E_M \\ 0 & 0 & 1 & -X_B \\ 0 & 0 & 0 & 1 \end{bmatrix}, \tag{A9, 10}$$

$$[M_{pn}] = \begin{bmatrix} \cos\gamma_{m_1} & 0 & \sin\gamma_{m_1} & -X_P \\ 0 & 1 & 0 & E_m \\ -\sin\gamma_{m_1} & 0 & \cos\gamma_{m_1} & -X_B \\ 0 & 0 & 0 & 1 \end{bmatrix}, \tag{A11}$$

$$[M_{w1p}] = \begin{bmatrix} 1 & 0 & 0 & 0 \\ 0 & \cos\phi_1 & -\sin\phi_1 & 0 \\ 0 & \sin\phi_1 & \cos\phi_1 & 0 \\ 0 & 0 & 0 & 1 \end{bmatrix}, \quad [M_{f1}] = \begin{bmatrix} 1 & 0 & 0 & H \\ 0 & \cos\phi_1' & \sin\phi_1' & 0 \\ 0 & -\sin\phi_1' & \cos\phi_1' & 0 \\ 0 & 0 & 0 & 1 \end{bmatrix}, \tag{A12}$$

$$\mathbf{r}_2^{(2)}(u_2, v_2) = [M_{w2m2}][M_{m2t2}]\mathbf{r}_{t2}^{(2)}, \quad \mathbf{n}_2^{(2)}(u_2, v_2) = [M_{w2m2}][M_{m2t2}]\mathbf{n}_{t2}^{(2)}, \tag{A13, 14}$$

$$\mathbf{r}_f^{(2)} = [M_{f2}]\mathbf{r}_2^{(2)} = \mathbf{r}_f^{(2)}(u_2, v_2,, \phi_2'), \quad \mathbf{n}_f^{(2)} = [M_{f2}]\mathbf{n}_2^{(2)} = \mathbf{n}_f^{(2)}(u_2, v_2,, \phi_2'), \tag{A15, 16}$$

$$\mathbf{r}_{t2}^{(2)}(u_2, v_2) = \begin{bmatrix} (r_{cG} - u_2\sin\phi_{BG})\cos v_2 \\ (r_{cG} - u_2\sin\phi_{BG})\sin v_2 \\ -u_2\cos\phi_{BG} \\ 1 \end{bmatrix}, \quad \mathbf{n}_{t2}^{(2)}(u_2, v_2) = \begin{bmatrix} \cos\phi_{BG}\cos v_2 \\ \cos\phi_{BG}\sin v_2 \\ \sin v_2 \\ 0 \end{bmatrix}, \tag{A17, 18}$$

$$[M_{m2t2}] = \begin{bmatrix} 1 & 0 & 0 & 0 \\ 0 & 1 & 0 & -V_2 \\ 0 & 0 & 1 & H_2 \\ 0 & 0 & 0 & 1 \end{bmatrix}, \quad [M_{w2m2}] = \begin{bmatrix} \cos\gamma_{m_2} & 0 & -\sin\gamma_{m_2} & 0 \\ 0 & 1 & 0 & 0 \\ \sin\gamma_{m_2} & 0 & \cos\gamma_{m_2} & -X_G \\ 0 & 0 & 0 & 1 \end{bmatrix}, \tag{A19, 20}$$

$$[M_{f2}] = \begin{bmatrix} -\cos\varphi'_2 & \sin\varphi'_2 & 0 & 0 \\ \sin\varphi'_2 & \cos\varphi'_2 & 0 & E \\ 0 & 0 & -1 & 0 \\ 0 & 0 & 0 & 1 \end{bmatrix}. \tag{A21}$$

APPENDIX B: NOMENCLATURE

$[C]$	damping matrix
e	projected transmission error
E	pinion offset
E	pinion offset
$\{f\}$	forcing term
F	forcing term
$\mathbf{h}$	direction cosine vector
H	pitch apex beyond the cross point
$[H]$	compliance matrix
i_c	pinion cutter tilt angle
i, j, k	triad of unit vectors of a co-ordinate system
I	mass moment of inertia term
J_c	swivel angle
k	stiffness term
$[K]$	stiffness matrix
$[L]$	co-ordinate transformation matrix
m	mass element
$[M]$	mass matrix
$\mathbf{n}$	surface normal vector
N_c	number of total contact cell
$\mathbf{q}$	displacement vector
Q_c	basic cradle setting
r_{cP}	pinion cutter point radius
r_{cG}	gear cutter point width
R_a	ratio of roll
S_l	co-ordinate system for dynamical formulation
t	time
T_r	modal displacement index
$\mathrm{w}_x, \mathrm{w}_y, \mathrm{w}_z$	angular displacement
x, y, z	translation displacement
X, Y, Z	co-ordinate axes
ζ	element of direction cosine
ξ	modal damping ratio
$\boldsymbol{\Phi}$	mode shape
ϕ_c	cradle rotation angle
ϕ_1	pinion rotation angle in generation, $R_a\phi_c$
φ'_1	pinion rotational angle in S_f
φ'_2	gear rotational angle in S_f
ϕ_{BP}	pinion cutter balde angle

ϕ_{BG} gear cutter blade angle
ω frequency (rad/s)

Subscripts

b bearing
f fixed co-ordinate system
G gear
l label for pinion ($l = 1$) or gear ($l = 2$)
P pinion
r modal number

Superscripts

l co-ordinate system for pinion ($l = 1$) or gear ($l = 2$)
T transpose